JOURNAL OF GEOPHYSICAL RESEARCH, VOL. 113, C10023, doi:10.1029/2007JC004244, 2008



# Mapping surface currents from HF radar radial velocity measurements using optimal interpolation

Sung Yong Kim,[1] Eric J. Terrill,[1] and Bruce D. Cornuelle[2]

Received 24 March 2007; revised 25 January 2008; accepted 17 March 2008; published 25 October 2008.

[1] An optimal interpolation (OI) method to compute surface vector current fields from radial velocity measurements derived from high-frequency (HF) radars is presented. The method assumes a smooth spatial covariance relationship between neighboring vector currents, in contrast to the more commonly used un-weighted least-squares fitting (UWLS) method, which assumes a constant vector velocity within a defined search radius. This OI method can directly compute any quantities linearly related to the radial velocities, such as vector currents and dynamic quantities (divergence and vorticity) as well as the uncertainties of those respective fields. The OI method is found to be more stable than the UWLS method and reduces spurious vector solutions near the baselines between HF radar installations. The OI method produces a covariance of the uncertainty of the estimated vector current fields. Three nondimensional uncertainty indices are introduced to characterize the uncertainty of the vector current at a point, representing an ellipse with directional characteristics. The vector current estimation using the OI method eliminates the need for multiple mapping steps and optimally fills intermittent coverage gaps. The effects of angular interpolation of radial velocities, a commonly used step in the preprocessing of radial velocity data prior to vector current computation in the UWLS method, are presented.

**Citation:** Kim, S. Y., E. J. Terrill, and B. D. Cornuelle (2008), Mapping surface currents from HF radar radial velocity measurements using optimal interpolation, *J. Geophys. Res.*, *113*, C10023, doi:10.1029/2007JC004244.

## 1. Introduction

[2] The Doppler shifts of backscattered radio signals from surface gravity waves are used to estimate the current component in the direction of the bearing angle of the radar cell (Figure 1). The radial velocities on the radar grid points are estimated using either beam forming or direction finding (e.g., MUSIC) [*Lipa and Barrick*, 1983; *Schmidt*, 1986; *Barrick and Lipa*, 1996, 1997; *de Paolo and Terrill*, 2007]. Radial velocities measured from multiple radars are combined into vector currents on a rectangular grid, which is called vector grid, using a variety of methods. This computation is an independent step from the radial current estimation algorithm, and is applicable to the data obtained by high-frequency (HF) radar systems (e.g., WERA, CODAR).

[3] An un-weighted least-squares fitting (UWLS) method has been used by many authors to extract the vector currents from the radial velocities [*Lipa and Barrick*, 1983; *Gurgel*, 1994; *Graber et al.*, 1997]. Implicit in this approach is an assumption of a uniform vector velocity producing the radial velocities within the search radius for a given vector grid point. In other words, the correlation of the vector current is assumed to be one everywhere within the search radius and zero outside. The method also assumes an unlimited signal variance, which may create spurious estimates when combining nearly aligned noisy radial velocities due to the singularity of the geometric covariance matrix (equation (6)). The terms "signal variance" and "error variance" are defined here as the expected variance of the surface currents and the expected observational error variance of the surface currents, respectively. In operation, spurious vector solutions most often occur near the baseline between two radars or near the maximum range. The segmented correlation function in the UWLS method can also produce a discontinuous current field. The proposed optimal interpolation (OI) method uses a correlation for the surface currents which more accurately describes the spatial relationship between radial velocity measurements.

[4] The uncertainty of the estimated vector current has historically been addressed in two ways. The geometric dilution of precision (GDOP), which is calculated from the inverse of the geometric covariance matrix, has been used as an indicator of uncertainty [*Lipa and Barrick*, 1983; *Chapman et al.*, 1997]. In a slightly different way, the geometric covariance matrix is built with the cosine and sine function of the bearing angle inversely weighted by the hourly standard deviation (HSTD) of radial velocities [*Gurgel*, 1994; *Lipa*, 2003]. Since the GDOP has different minimum depending on the number of available radial velocities (see Appendix A), and the HSTD inversely weighted radial velocities follow different statistics compared to the

[1] Marine Physical Laboratory, Scripps Institution of Oceanography, La Jolla, California, USA.
[2] Physical Oceanography Research Division, Scripps Institution of Oceanography, La Jolla, California, USA.


0148-0227/08/2007JC004244$09.00

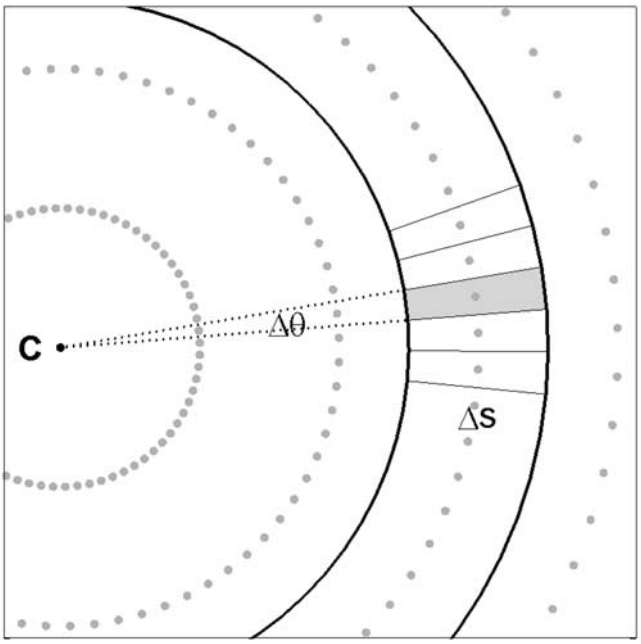


**Figure 1.** Radar grid structure for the radar located at point C. Each radar grid point (gray dot) is the center of a radar cell with the range resolution ($\Delta s$) and the azimuthal resolution ($\Delta\theta$). A radar cell is the intersection of a range bin (annulus with thick curves) with an azimuthal bin (dotted lines).

raw (unconditioned) radial velocities, a unified definition of the uncertainty would be useful. In the OI method, an error covariance matrix is computed from the HSTD of radial velocities or the assumed error variance to provide an uncertainty for regularization. Three uncertainty indices are introduced as a normalized indicator for the quality of the solution.

[5] This paper is composed of four parts. First, we start with a general form of least-squares fitting, weighted least-squares fitting (WLS), which is used to calculate the vector currents. We then show how to obtain the UWLS formula by allowing the signal variance to be infinite. Next, we describe the OI method using an averaging kernel with infinite basis (section 2.2), the algebraic derivation of the UWLS method from the OI method with finite basis (section 2.3), the implementation of the OI method (section 2.4), and the determination of parameters in the UWLS and OI methods (section 2.5). In the third part, the basic statistics of radial velocities and the radar uncertainty are addressed (section 3). Finally, examples and discussions using both methods are summarized (section 4).

## 2. Methods

[6] The mean radial velocity ($r$) is the temporal average of $N$ radial velocities ($r_0$) estimated from cross spectra of the backscattered signals during a given time span and in a given radar cell. (The time span in this paper is an hour.) The hourly standard deviation (HSTD, $\epsilon$) of the radial velocities is related to the uncertainty of the mean value (i.e., standard error):

$$\epsilon = \sqrt{\frac{1}{N}\sum_{i=1}^{N}\left(r_0^i - r\right)^2}, \tag{1}$$

where $r_0^i$ is the radial velocity obtained at the $i$th time, and $N$ is the subsampling rate during the given time span. The radial velocity referred to in this paper is the hourly mean radial velocity ($r$), and its HSTD ($\epsilon$) will be used in the construction of the error covariance of radial velocities.

### 2.1. Least-Squares Fitting

[7] The weighted least-squares fitting (WLS, [*Wunsch*, 1996]) method to estimate the vector current ($\mathbf{u}$, $2 \times 1$ elements) at a vector grid point ($x_k$, $y_k$) assumes that each radial velocity is a linear combination of the vector current components. The radial velocities ($\mathbf{r}$, $L \times 1$ elements) within the search radius ($d_0$) of the vector grid point are expressed with the projection matrix ($\mathbf{G_a}$, $L \times 2$ elements) and the vector current ($\mathbf{u}$):

$$\mathbf{r} = \mathbf{G_a}\mathbf{u} + \mathbf{n_a}, \tag{2}$$

where

$$\mathbf{G_a} = \begin{bmatrix} \mathbf{g}_1^{\mathrm{T}} \\ \mathbf{g}_2^{\mathrm{T}} \\ \vdots \\ \mathbf{g}_L^{\mathrm{T}} \end{bmatrix} = \begin{bmatrix} \cos\theta_1 & \sin\theta_1 \\ \cos\theta_2 & \sin\theta_2 \\ \vdots & \vdots \\ \cos\theta_L & \sin\theta_L \end{bmatrix}, \mathbf{r} = \begin{bmatrix} r_1 \\ r_2 \\ \vdots \\ r_L \end{bmatrix}, \tag{3}$$

$\mathbf{g}_i = [\cos\theta_i \ \sin\theta_i]^{\mathrm{T}}$, $\theta_i$ denotes the bearing angle at the $i$th radar grid point ($x_i$, $y_i$) measured counterclockwise from East, $\mathbf{n_a}$ is the residual ($L \times 1$ elements) when the radial velocities are fit by a single vector current, and $L$ is the number of radial velocities within in the search radius ($^{\mathrm{T}}$ denotes the matrix transpose). The least-squares estimate for the vector current is

$$\hat{\mathbf{u}} = \left(\mathbf{G_a}^{\mathrm{T}}\mathbf{R}^{-1}\mathbf{G_a} + \mathbf{P}^{-1}\right)^{-1}\mathbf{G_a}^{\mathrm{T}}\mathbf{R}^{-1}\mathbf{r}. \tag{4}$$

[8] The model covariance matrix ($\mathbf{P} \equiv \langle \mathbf{u}\mathbf{u}^{\mathrm{T}} \rangle$) is the expected covariance of the unknown velocity, where $\langle\cdot\rangle$ denotes the expected value. The error covariance matrix ($\mathbf{R} \equiv \langle \mathbf{n_a}\mathbf{n_a}^{\mathrm{T}} \rangle$) is the covariance matrix of the measurement uncertainty. In simple least-squares fitting, both $\mathbf{P}$ and $\mathbf{R}$ are assumed to be scaled identity matrices:

$$\mathbf{P} = \sigma_s^2\mathbf{I} \text{ and } \mathbf{R} = \sigma_r^2\mathbf{I}. \tag{5}$$

[9] With the assumption of infinite signal variance ($\sigma_s^2 = \infty$) and unit error variance ($\sigma_r^2 = 1$), the WLS method matches the UWLS method, which is the standard method in the estimate of vector currents [*Lipa and Barrick*, 1983; *Gurgel*, 1994; *Graber et al.*, 1997]. The UWLS method also assumes constant vector currents within the search radius ($d_0$) of the vector grid point, and the estimate becomes

$$\hat{\mathbf{u}} = \left(\mathbf{G_a}^{\mathrm{T}}\mathbf{G_a}\right)^{-1}\mathbf{G_a}^{\mathrm{T}}\mathbf{r}, \tag{6}$$

where $\mathbf{G_a}^{\mathrm{T}}\mathbf{G_a}$ is called the geometric covariance matrix ($2 \times 2$ elements), of which the inverse matrix is discussed with GDOP in Appendix A.

### 2.2. Averaging Kernel With Infinite Basis

[10] To begin a more general discussion of the computation of the vector current field, we consider the sampling function. The radial velocity (**r**) is sampled by the kernel (**w**) over a region ($\Omega$) surrounding the nominal radar grid point ($x_i$, $y_i$) from a spatially continuous current field (**u**).

$$\mathbf{r}(x_i, y_i) = \iint_{\Omega} \mathbf{w}(x_i, y_i, x, y)^{\mathrm{T}} \mathbf{u}(x, y) \mathrm{d}x\mathrm{d}y + \mathbf{n}, \tag{7}$$

where $\mathbf{r} = \mathbf{r}(x_i, y_i)$, $\mathbf{w} = \mathbf{w}(x_i, y_i, x, y)$, $\mathbf{u} = \mathbf{u}(x, y)$, and **n** is the measurement error of the radial velocity.

[11] The kernel represents the sensitivity of the observed radial velocities to the surface vector current in the backscattering region. In other words, the kernel specifies the average over range and bearing angle of the HF radar measurements. If the bearing angle is constant over the local domain where the kernel ($\mathbf{w}(x_i, y_i, x, y)$) is defined, the kernel can be factored into separate coverage and angle components:

$$\mathbf{r}(x_i, y_i) = \iint_{\Omega} w(x_i, y_i, x, y) \mathbf{g}(x_i, y_i)^{\mathrm{T}} \mathbf{u}(x, y) \mathrm{d}x\mathrm{d}y + \mathbf{n}, \tag{8}$$

where $\mathbf{g}_i = \mathbf{g}(x_i, y_i) = [\cos\theta_i \ \sin\theta_i]^{\mathrm{T}}$, and $\theta_i$ denotes the bearing angle at the radar grid point. The weighting of the kernel ($w(x_i, y_i, x, y)$) is a function of the local radar grid point ($x_i$, $y_i$) and the point ($x$, $y$) being sampled. The kernel (**w**) is normalized to unity,

$$\iint_{\Omega} |\mathbf{w}(x_i, y_i, x, y)| \mathrm{d}x\mathrm{d}y = 1. \tag{9}$$

[12] The vector grid points to be mapped can be considered individually or as a grouped matrix. In this paper, the UWLS and OI methods are described one by one.

[13] The OI estimates [*Bretherton et al.*, 1976] for the vector current ($\hat{\mathbf{u}}$), the a posterior uncertainty matrix ($\hat{\mathbf{P}}$), and the normalized uncertainty matrix ($\hat{\boldsymbol{\chi}}$) at a single point ($x_k$, $y_k$) are

$$\hat{\mathbf{u}} = \mathrm{cov}_{\mathrm{dm}}^{\mathrm{T}} \mathrm{cov}_{\mathrm{dd}}^{-1} \mathbf{r}, \tag{10}$$

$$\hat{\mathbf{P}} = \mathrm{cov}_{\mathrm{mm}} - \mathrm{cov}_{\mathrm{dm}}^{\mathrm{T}} \mathrm{cov}_{\mathrm{dd}}^{-1} \mathrm{cov}_{\mathrm{dm}}, \tag{11}$$

and

$$\hat{\boldsymbol{\chi}} = \mathbf{I} - \mathrm{cov}_{\mathrm{mm}}^{-1} \mathrm{cov}_{\mathrm{dm}}^{\mathrm{T}} \mathrm{cov}_{\mathrm{dd}}^{-1} \mathrm{cov}_{\mathrm{dm}}, \tag{12}$$

where these three matrices are:

$$(\mathrm{cov}_{\mathrm{dm}})_{ik} = \langle \mathbf{r}_i \mathbf{u}^{\mathrm{T}} \rangle = \iint_{\Omega} w_i \mathbf{g}_i^{\mathrm{T}} \langle \mathbf{u}(x, y) \mathbf{u}^{\mathrm{T}}(x_k, y_k) \rangle \mathrm{d}x\mathrm{d}y, \tag{13}$$

$$(\mathrm{cov}_{\mathrm{dd}})_{ij} = \langle \mathbf{r}_i \mathbf{r}_j^{\mathrm{T}} \rangle + \langle \mathbf{n}_i \mathbf{n}_j^{\mathrm{T}} \rangle = \iint_{\Omega'} \iint_{\Omega} w_i w_j \mathbf{g}_i^{\mathrm{T}} \langle \mathbf{u}(x, y) \mathbf{u}^{\mathrm{T}}(x', y') \rangle \mathbf{g}_j \mathrm{d}x\mathrm{d}y\mathrm{d}x'\mathrm{d}y' + \langle \mathbf{n}_i \mathbf{n}_j^{\mathrm{T}} \rangle, \tag{14}$$

and

$$(\mathrm{cov}_{\mathrm{mm}})_{kk} = \langle \hat{\mathbf{u}}_k \hat{\mathbf{u}}_k^{\mathrm{T}} \rangle, \tag{15}$$

where $(\mathrm{cov}_{\mathrm{dm}})_{ik}$ and $(\mathrm{cov}_{\mathrm{dd}})_{ij}$ denote the components at the $i$th row and $k$th (or $j$th) column of the data-model covariance matrix ($\mathrm{cov}_{\mathrm{dm}}$) and the data-data covariance matrix ($\mathrm{cov}_{\mathrm{dd}}$), respectively. The measurement uncertainty covariance matrix ($\langle \mathbf{n}_i \mathbf{n}_j^{\mathrm{T}} \rangle$) is a diagonal matrix if the radial velocity errors are independent. The error covariance is assumed to be

$$\langle \mathbf{n}_i \mathbf{n}_j^{\mathrm{T}} \rangle = \delta_{ij} \sigma_r^2, \tag{16}$$

where $\sigma_r^2$ includes the average measurement uncertainty ($\gamma^2$) of the radial velocity and the possibly time-dependent standard error ($\epsilon^2/N$) of the mean radial velocity for $N$ samples per hour:

$$\sigma_r^2 = \gamma^2 + \frac{\epsilon^2}{N}. \tag{17}$$

[14] The number of samples during an hour in the radar operation is not recorded for each radar cell and varies in time and space between at least one and at most six in our data set ($1 \leq N \leq 6$).

[15] The average measurement uncertainty ($\gamma^2$) of the radial velocity is the sum of the representational error of the model [*Lorenc*, 1986; *Daley*, 1993] and the errors in the radar measurements, and can be estimated by the variance of the sum of the radial velocities measured at nearby points by two opposing radars (section 3.3).

[16] Although the radar measurement is not local, the form of the kernel (**w**) is not well-defined. Therefore for simplicity the averaging kernel is hereafter assumed to be a delta function in space:

$$w_i = \delta(\mathbf{x} - \mathbf{x}_i). \tag{18}$$

[17] The data-model covariance matrix (equation (13)) and the data-data covariance matrix (equation (14)) are

$$(\mathrm{cov}_{\mathrm{dm}})_{ik} = \mathbf{g}_i^{\mathrm{T}} \langle \mathbf{u}_i \mathbf{u}_k^{\mathrm{T}} \rangle \tag{19}$$

and

$$(\mathrm{cov}_{\mathrm{dd}})_{ij} = \mathbf{g}_i^{\mathrm{T}} \langle \mathbf{u}_i \mathbf{u}_j^{\mathrm{T}} \rangle \mathbf{g}_j + \delta_{ij} \sigma_r^2. \tag{20}$$

[18] In this case each radial velocity can be considered as a point observation. The representational error may be adjusted to account for the covariance scale and the assumption that the kernel is a delta function.

### 2.3. Derivation of UWLS From OI

[19] The OI method is a general approach to calculate vector currents. One can obtain the UWLS method from the OI method by making several simplifying assumptions. By default, the OI method assumes a continuous current field so that the radial velocities (**r**, $M \times 1$ elements) are the

projection of the collocated vector currents ($\mathbf{u}$) along the bearing angle ($M$ is the total number of radial velocities):

$$\mathbf{r} = \mathbf{G}\mathbf{u}, \tag{21}$$

where $\mathbf{u}$ represents the vector currents at the radar grid points ($2M \times 1$ elements) and the projection matrix ($\mathbf{G}$, $M \times 2M$ elements) is

$$\mathbf{G} = \begin{bmatrix} \mathbf{g}_1^{\mathrm{T}} & \mathbf{0} & \mathbf{0} & \mathbf{0} \\ \mathbf{0} & \mathbf{g}_2^{\mathrm{T}} & \mathbf{0} & \mathbf{0} \\ \mathbf{0} & \mathbf{0} & \ddots & \mathbf{0} \\ \mathbf{0} & \mathbf{0} & \mathbf{0} & \mathbf{g}_M^{\mathrm{T}} \end{bmatrix}. \tag{22}$$

[20] The continuous current field ($\mathbf{u}$) may be parameterized by a finite set of values ($\mathbf{m}$), and transformed to the radial velocities at the radar grid points by the interpolation matrix ($\mathbf{F_r}$):

$$\mathbf{u} = \mathbf{F_r}\mathbf{m}. \tag{23}$$

[21] Therefore the radial velocities are

$$\mathbf{r} = \mathbf{G}\mathbf{F_r}\mathbf{m} + \mathbf{n} = \bar{\mathbf{G}}\mathbf{m} + \mathbf{n}, \tag{24}$$

where $\bar{\mathbf{G}} \equiv \mathbf{G}\mathbf{F_r}$ and $\mathbf{F_r}$ can represent a Fourier series expansion, a normal mode expansion [*Lipphardt et al.*, 2000; *Kaplan and Lekien*, 2007], or an interpolation from a regular grid of vector current values. As before, $\mathbf{n}$ is the residual when the vector current is fit to the parameters. The use of the current values at the vector grid points as the parameters for a linear spline basis set makes for the simplest comparison to the discrete least-squares fitting method.

[22] If the model is described with a finite basis as in equation (24) [*Davis*, 1985], the estimated vector current ($\hat{\mathbf{u}}$, equation (10)) can be determined from the optimized parameters:

$$\hat{\mathbf{u}} = \mathbf{F_g}\hat{\mathbf{m}}, \tag{25}$$

where $\mathbf{F_g}$ is the mapping matrix of the vector currents to the vector grid point.

$$\hat{\mathbf{u}} = \mathbf{F_g}\mathbf{P}\bar{\mathbf{G}}^{\mathrm{T}}\left(\bar{\mathbf{G}}\mathbf{P}\bar{\mathbf{G}}^{\mathrm{T}} + \mathbf{R}\right)^{-1}\mathbf{r} \tag{26}$$

$$= \mathbf{F_g}\left(\bar{\mathbf{G}}^{\mathrm{T}}\mathbf{R}^{-1}\bar{\mathbf{G}} + \mathbf{P}^{-1}\right)^{-1}\bar{\mathbf{G}}^{\mathrm{T}}\mathbf{R}^{-1}\mathbf{r}. \tag{27}$$

[23] If the parameters ($\hat{\mathbf{m}}$) in equation (23) are the estimated vector currents ($\hat{\mathbf{u}}$) on the vector grid points, then $\mathbf{F_g}$ in equation (25) becomes the identity matrix, and the model covariance matrix ($\mathbf{P}$) becomes $\langle \mathbf{u}\mathbf{u}^{\mathrm{T}} \rangle$. Equations (26) and (27) are interchangeable by the matrix inversion lemma [*Golub and Van Loan*, 1996]. In a similar way, the a posterior uncertainty matrix ($\hat{\mathbf{P}}$, equation (11)) with a finite basis at a vector grid point is derived corresponding to equations (26) and (27) as

$$\hat{\mathbf{P}} = \mathbf{F_g}\mathbf{P}\mathbf{F_g}^{\mathrm{T}} - \mathbf{F_g}\mathbf{P}\bar{\mathbf{G}}^{\mathrm{T}}\left(\bar{\mathbf{G}}\mathbf{P}\bar{\mathbf{G}}^{\mathrm{T}} + \mathbf{R}\right)^{-1}\bar{\mathbf{G}}\mathbf{P}^{\mathrm{T}}\mathbf{F_g}^{\mathrm{T}} \tag{28}$$

$$= \mathbf{F_g}\left(\bar{\mathbf{G}}^{\mathrm{T}}\mathbf{R}^{-1}\bar{\mathbf{G}} + \mathbf{P}^{-1}\right)^{-1}\mathbf{F_g}^{\mathrm{T}}. \tag{29}$$

[24] For comparison, the a posteriori uncertainty matrices in the WLS and UWLS methods are

$$\hat{\mathbf{P}} = \left(\mathbf{G_a}^{\mathrm{T}}\mathbf{R}^{-1}\mathbf{G_a} + \mathbf{P}^{-1}\right)^{-1} \tag{30}$$

and

$$\hat{\mathbf{P}} = \left(\mathbf{G_a}^{\mathrm{T}}\mathbf{G_a}\right)^{-1}, \tag{31}$$

respectively.

[25] The normalized uncertainty matrix ($\varphi$) is introduced in order to compare the uncertainty in the estimate between the UWLS and OI methods. The corresponding normalized uncertainty matrix in the OI method is the a posteriori uncertainty matrix (equation (29)) divided by the observational error variance ($\sigma_r^2$):

$$\varphi = \left(\bar{\mathbf{G}}^{\mathrm{T}}\bar{\mathbf{G}} + \mathbf{P}^{-1}\sigma_r^2\right)^{-1}, \tag{32}$$

(recall that $\mathbf{R} = \sigma_r^2\mathbf{I}$). On the other hand, since the UWLS method implies the unit error variance (1 cm$^2$ s$^{-2}$), the normalized uncertainty matrix is exactly the same as equation (31):

$$\varphi = \left(\mathbf{G_a}^{\mathrm{T}}\mathbf{G_a}\right)^{-1}. \tag{33}$$

[26] Motivated by the convenience of a unified definition of the uncertainty, we suggest an alternative nondimensional uncertainty index matrix ($\hat{\chi}$, equation (12)), which is normalized by the signal variance ($\sigma_s^2$) instead of the error variance ($\sigma_r^2$). For the OI method, this is the a posteriori uncertainty covariance matrix normalized by the a priori model covariance ($\mathbf{P}$):

$$\hat{\chi} \equiv \mathbf{P}^{-1/2}\left(\mathbf{P} - \mathbf{P}\bar{\mathbf{G}}^{\mathrm{T}}\left(\bar{\mathbf{G}}\mathbf{P}\bar{\mathbf{G}}^{\mathrm{T}} + \mathbf{R}\right)^{-1}\bar{\mathbf{G}}\mathbf{P}^{\mathrm{T}}\right)\mathbf{P}^{-1/2}. \tag{34}$$

[27] This nondimensional uncertainty index matrix does not exist in the UWLS method due to the assumption of the infinite signal variance ($\sigma_s^2 = \infty$), so the a priori model covariance matrix is not meaningful.

### 2.4. Implementing Optimal Interpolation

[28] This section describes the approach taken to apply the OI method to the radial velocity data. The estimation of the vector current ($\hat{\mathbf{u}}$, equation (10)) requires the data-model covariance matrix (equation (19)) and the data-data covariance matrix (equation (20)):

$$(\mathrm{cov_{dm}})_{ik} = \mathbf{g}_i^{\mathrm{T}}\sigma_s^2(x_k, y_k)\rho(\Delta x_{ik}, \Delta y_{ik}) \tag{35}$$

and

$$(\mathrm{cov_{dd}})_{ij} = \mathbf{g}_i^{\mathrm{T}}\sigma_s^2(x_k, y_k)\rho(\Delta x_{ij}, \Delta y_{ij})\mathbf{g}_j + \delta_{ij}\sigma_r^2, \tag{36}$$

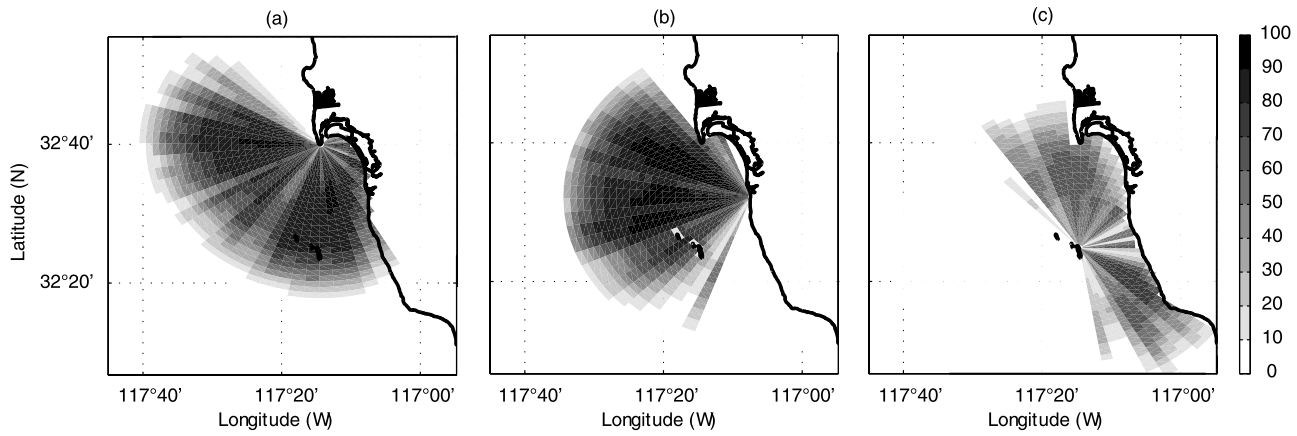


**Figure 2.** Percent availability of the radial velocities at each radar site during the 2-year study period (April 2003 – March 2005). (a) SDPL. (b) SDBP. (c) SDCI.

where $\mathbf{g}_i = [\cos\theta_i \ \sin\theta_i]^T$, $(\Delta x_{ik}, \Delta y_{ik}) = (x_i - x_k, y_i - y_k)$, $(\Delta x_{ij}, \Delta y_{ij}) = (x_i - x_j, y_i - y_j)$, and $\sigma_s^2(x_k, y_k)$ is the expected variance of surface currents at $(x_k, y_k)$. $\rho(\Delta x, \Delta y)$ is the correlation function of the surface currents. Both exponential and Gaussian correlation functions are widely used.

Exponential:

$$\rho(\Delta x, \Delta y) = \exp\left(-\sqrt{\left(\frac{\Delta x}{\lambda_x}\right)^2 + \left(\frac{\Delta y}{\lambda_y}\right)^2}\right), \tag{37}$$

Gaussian:

$$\rho(\Delta x, \Delta y) = \exp\left(-\left(\frac{\Delta x}{\lambda_x}\right)^2 - \left(\frac{\Delta y}{\lambda_y}\right)^2\right), \tag{38}$$

where $\lambda_x$ and $\lambda_y$ are the decorrelation length scales in the $x$- and $y$-directions, respectively.

[29] The normalized uncertainty matrix ($\boldsymbol{\varphi}$) and the uncertainty index matrix ($\hat{\boldsymbol{\chi}}$) are

$$\boldsymbol{\varphi} = \frac{1}{\sigma_r^2}\left(\mathrm{cov}_{\mathrm{mm}} - \mathrm{cov}_{\mathrm{dm}}^{\mathrm{T}}\mathrm{cov}_{\mathrm{dd}}^{-1}\mathrm{cov}_{\mathrm{dm}}\right) \tag{39}$$

and

$$\hat{\boldsymbol{\chi}} = \frac{1}{\sigma_s^2}\left(\mathrm{cov}_{\mathrm{mm}} - \mathrm{cov}_{\mathrm{dm}}^{\mathrm{T}}\mathrm{cov}_{\mathrm{dd}}^{-1}\mathrm{cov}_{\mathrm{dm}}\right). \tag{40}$$

### 2.5. Definition of Parameters

[30] Several parameters must be chosen, depending on the method: the search radius ($d_0$), the decorrelation length scales ($\lambda_x$ and $\lambda_y$), the signal variance ($\sigma_s^2$), and the data error variance ($\sigma_r^2$). These parameters are functions of the range resolution ($\Delta s$) of the radar and the vector grid resolution ($\Delta x$ and $\Delta y$). The vector grid resolution is determined by the spatial scales needed to resolve the surface currents of interest and limited by the radar resolution.

[31] The implied correlation function of the surface currents in the least-squares fitting (UWLS and WLS) methods is one within the search radius ($d_0$) and zero outside. The search radius is typically chosen to be similar to the range resolution ($\Delta s$) of the radar, and so the observations at adjacent radar cells in range and azimuthal directions are assumed to be independent. In contrast to the least-squares fitting method, the correlation function of the OI method is controlled by the decorrelation length scales ($\lambda_x$ and $\lambda_y$), which are set according to the scales of the surface currents to be resolved.

[32] In order to avoid over-smoothing the data, the decorrelation length scale should be no longer than the expected length scale of the surface current. To resolve the variability, the grid resolution should be smaller than the expected length scale. In order to avoid too much redundancy, the four times of the vector grid resolution is suggested as an upper bound of the length scale, and the vector grid resolution is set to the length scale as the lower bound:

$$\Delta x \le \lambda_x \le 4\Delta x \text{ and } \Delta y \le \lambda_y \le 4\Delta y. \tag{41}$$

[33] The radial velocities measured by the long range and short range high-frequency radars in Southern California are used to examine how the sensitivity and variability of the estimated current field depend on the decorrelation length scale. Although the variability of the estimate currents depends on the decorrelation length scale, the overall current variability is found to be varying only weakly within the suggested range.

[34] In practice the spatial scale of the surface currents is poorly known in advance, so these choices may be refined as data are collected. Since the size of the square matrix in the OI method is the number of radial velocities, restricting the search range ($d_0$) saves calculation time.

## 3. Observations

### 3.1. Coverage

[35] While the approach described here can be applied to any radar systems, the settings and data from an array of 25 MHz direction-finding style SeaSonde systems (Codar Ocean Sensors, Palo Alto, CA) are used. The radar cell is defined by a range resolution ($\Delta s$) of 1.49 km and an azimuthal resolution ($\Delta\theta$) of 5° (Figure 1). The maximum range is less than 45 km and the effective bearing angles of individual radars are different due to the coastline geometry. The fractional availability of radial velocities of each radar

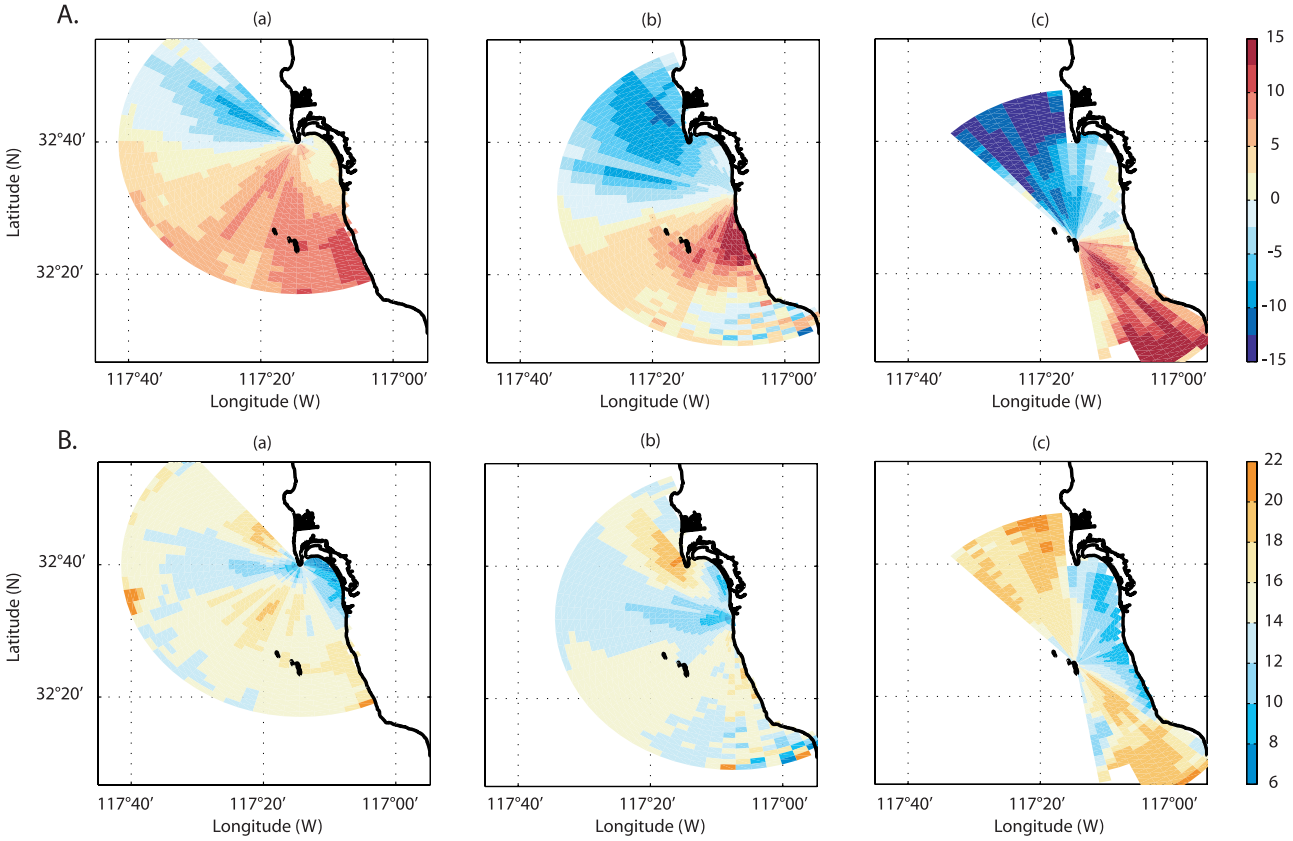


**Figure 3.** A. The time mean of the radial velocities (cm $s^{-1}$). A negative (positive) velocity indicates the flow toward (away from) the radar. B. The standard deviations of the radial velocities (cm $s^{-1}$). Column (a): SDPL. Column (b): SDBP. Column (c): SDCI.

during 2 years duration (April 2003–March 2005) is shown in Figure 2. The timeline of available radial velocities at each radar site is addressed elsewhere (Figure 3a in *Kim et al.* [2007]). The radial velocities calculated with the measured antenna response function at three sites are analyzed in this paper: Point Loma (SDPL), Border Field State Park on the U.S.-Mexico Border (SDBP), and Coronado Islands (SDCI).

### 3.2. Basic Statistics

[36] The 2-year mean of the radial velocities measured by each radar is shown in Figure 3A. Since the radial velocity at a radar grid point is the projection of the vector current in the bearing angle, the contribution of the current component normal to the bearing angle is zero. The mean of the

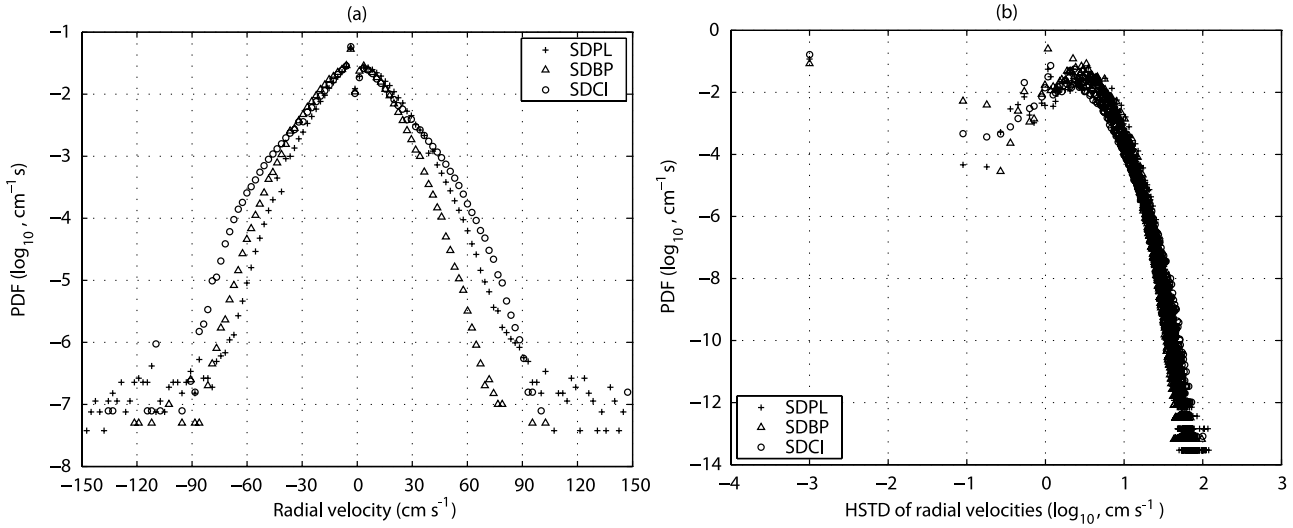


**Figure 4.** Probability density functions (PDFs) of (a) the radial velocities and (b) their hourly standard deviations (HSTDs) at each radar site during the 2-year study period (April 2003–March 2005).

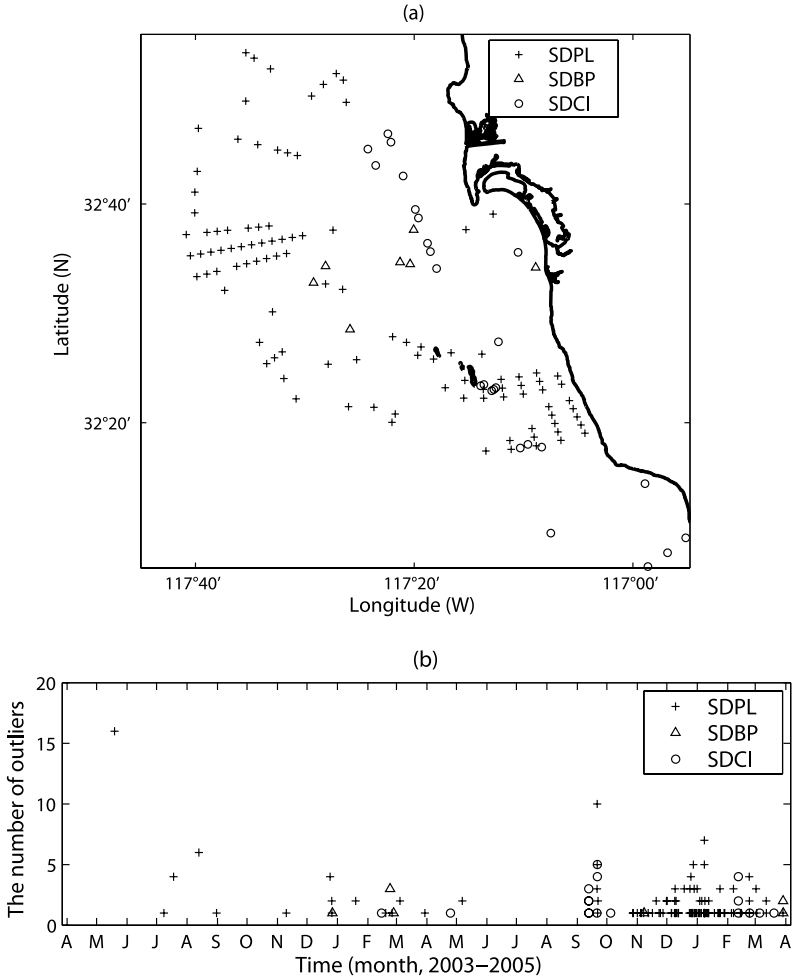


**Figure 5.** (a) The spatial distribution and (b) the temporal occurrence of radial velocities with magnitudes greater than 90 cm $s^{-1}$.

observed radial velocities is consistent with the typical south-eastward currents on this region [*Kim et al.*, 2007].

[37] The standard deviation (RMS) of radial velocities for each radar is shown in Figure 3B. Typical RMS of the surface current is ~10 cm $s^{-1}$ in nearshore and ~20 cm $s^{-1}$ in offshore, respectively. Regions of low radial velocity variance are seen for all sites where the major axes of the surface current ellipses are normal the directions of the radial velocities. Higher RMS near land may result from abrupt changes of the radar signal strength due to land shadowing and the antenna response function. However, the higher values west of Point Loma for all three radar sites do not completely fit this explanation and need a separate investigation.

[38] The probability density functions (PDFs) of the radial velocities measured by each radar during the 2-year study period, shown in Figure 4a, roughly resemble Gaussian distributions with fat tails. All three sites show similar e-folding scales and tails in the PDFs. The radial velocities in the tail of the PDF ($|r| > 90$ cm $s^{-1}$) are typically located at the edge of the radar coverage region, and therefore can be interpreted as outliers. Since the resolutions ($\Delta r$) of the radial velocity due to the first-order sea echo are 2.39, 2.29, and 2.36 cm $s^{-1}$ for SDPL, SDBP, and SDCI, respectively, there are discontinuities in the PDFs where the magnitude of the radial velocity is less than 2 cm $s^{-1}$.

[39] The PDFs in log scale of the HSTD of the radial velocities are shown in Figure 4b. The optimal histogram bin size ($w$) of the HSTD is given by the formula [*Scott*, 1979]

$$w = 3.49ab^{-1/3}, \tag{42}$$

where $a$ and $b$ denote the standard deviation of the HSTD and the number of available HSTD, respectively. The optimal histogram bin sizes are 0.07, 0.06, and 0.09 cm $s^{-1}$ for each site. Most of the HSTD vary between 0.5 and 5 cm $s^{-1}$, with upper bounds of about 120 cm $s^{-1}$. The means of the HSTD are 5.47, 4.65, and 4.64 cm $s^{-1}$ for each site. The mean HSTD is an estimate of the error variance of the surface currents. Since the number of samples ($N$) in each HSTD estimate is only known in a range ($1 \leq N \leq 6$), we assume that the time-dependent standard error is about 9 $cm^2$ $s^{-2}$ as a constant, corresponding to $N = 3$.

[40] The spatial and temporal distributions of radial velocities with magnitudes greater than 90 cm $s^{-1}$ are shown in Figures 5a and 5b, respectively. They are located in the distant range bins of SDPL and SDCI sites and along the edge of the azimuthal bin of the measured beam pattern of SDCI site. Some of the radial velocities with large magnitudes in SDBP site may not necessarily be outliers.

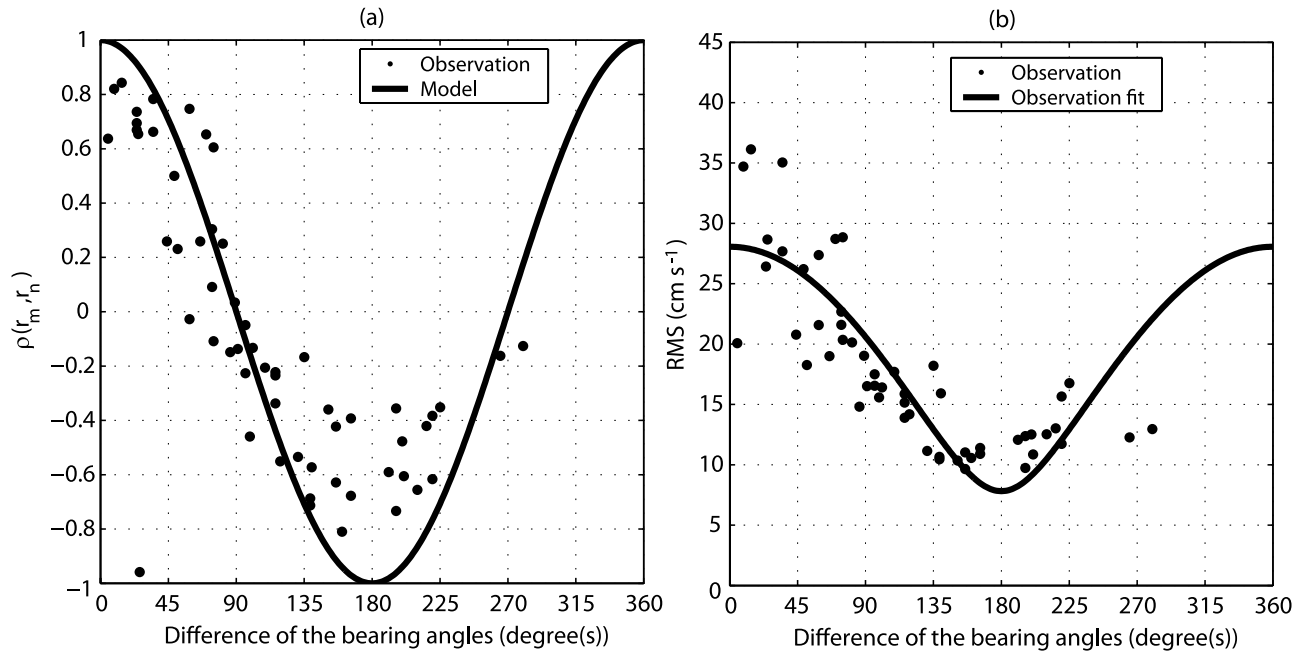


**Figure 6.** (a) Correlation coefficients of 58 radial velocity pairs ($\mathbf{r}_n$, $\mathbf{r}_m$) nearby radar grid points (points separated by less than 150 m) and the model correlation coefficients as a cosine function of the difference between bearing angles ($\gamma^2 = 0$). (b) The variance of the sum of nearby radial velocity pairs is fitted with a cosine square function, and the RMS error of the sum of the oppositely directed radial velocities is 7.8 cm $s^{-1}$ ($\gamma$ = 5.5 cm $s^{-1}$). The difference of the bearing angles is measured from one bearing angle in clockwise to the other.

The occurrences of outliers are more frequent during the winter than the summer.

[41] The two-dimensional joint PDF of radial velocities ($r$) and their HSTDs ($\epsilon$) at each radar site shows that there is no significant correlation between them:

$$P(r, \epsilon) \approx P(r)P(\epsilon). \tag{43}$$

The HSTDs of the radial velocities with magnitudes less than 30 cm $s^{-1}$ have roughly chi-square distributions.

### 3.3. Validation of Radial Velocities

[42] One method for determining the uncertainty of the radar measurements is the comparison of nearby radial velocities from two radars. Three requirements are recommended to find the pairs of radial velocities for this validation: The radar grid points where the radial velocities are measured are nearly collinear with the radar sites, separated by less than the radar range resolution, and nearly equidistant from the two sites. In the ideal case where the vector current is the same in both radar cells (or at coincident radar grid points), the correlation coefficients of those pairs would be a function of the difference between bearing angles. The two radial velocity measurements are

$$r_1(t) = \mathbf{g}_1^{\mathrm{T}}\mathbf{u}_1(t) + \epsilon_1(t) = u_1(t)\cos\theta_1 + v_1(t)\sin\theta_1 + \epsilon_1(t), \tag{44}$$

$$r_2(t) = \mathbf{g}_2^{\mathrm{T}}\mathbf{u}_2(t) + \epsilon_2(t) = u_2(t)\cos\theta_2 + v_2(t)\sin\theta_2 + \epsilon_2(t), \tag{45}$$

where $r_i$ denotes the measured radial velocity, $\mathbf{g}_i = [\cos\theta_i \ \sin\theta_i]^{\mathrm{T}}$ is the directional unit vector, $\theta_i$ is the bearing angle, $\epsilon_i$ is the radial measurement error at the $i$th radar, and $\mathbf{u}_i = [u_i \ v_i]^{\mathrm{T}}$ is the vector components of the surface current, so $\mathbf{g}_i^{\mathrm{T}}\mathbf{u}_i$ is an inner product ($i$ = 1, 2). Assuming the measurement errors are independent ($\langle\epsilon_1\epsilon_2^{\mathrm{T}}\rangle = 0$), the covariance of a pair of radial velocities is

$$\langle r_1 r_2^{\mathrm{T}}\rangle = \mathbf{g}_1^{\mathrm{T}}\langle\mathbf{u}_1\mathbf{u}_2^{\mathrm{T}}\rangle\mathbf{g}_2 = [\cos\theta_1 \quad \sin\theta_1]\ \langle\mathbf{u}_1\mathbf{u}_2^{\mathrm{T}}\rangle\begin{bmatrix}\cos\theta_2\\ \sin\theta_2\end{bmatrix}. \tag{46}$$

[43] If $\langle\mathbf{u}_1\mathbf{u}_2^{\mathrm{T}}\rangle = \sigma^2\mathbf{I}$, so $u$ and $v$ are independent with same variance, then the covariance is

$$\langle r_1 r_2^{\mathrm{T}}\rangle = \sigma^2(\cos\theta_1\cos\theta_2 + \sin\theta_1\sin\theta_2) = \sigma^2\cos(\theta_1 - \theta_2). \tag{47}$$

Converting the covariance to the correlation coefficient,

$$\rho(r_1, r_2) = \frac{\langle r_1 r_2^{\mathrm{T}}\rangle}{\sqrt{\langle r_1^2\rangle}\sqrt{\langle r_2^2\rangle}} = \frac{\sigma^2}{\sigma^2 + \gamma^2}\cos(\theta_1 - \theta_2), \tag{48}$$

where $\langle r_1^2\rangle = \langle r_2^2\rangle = \sigma^2 + \gamma^2$ and $\langle\epsilon_1^2\rangle = \langle\epsilon_2^2\rangle = \gamma^2$.

[44] From the observed radial velocities, 58 pairs are selected for which the distance between the pair of radar

**Table 1.** Comparisons of the Singularity in the Inversion of the Covariance Matrix and the Structure of the Correlation Function for the UWLS, WLS, and OI Methods

| | UWLS | WLS | OI |
|---|---|---|---|
| Singularity | singular | nonsingular | nonsingular |
| Correlation function | uniform | uniform | nonuniform |

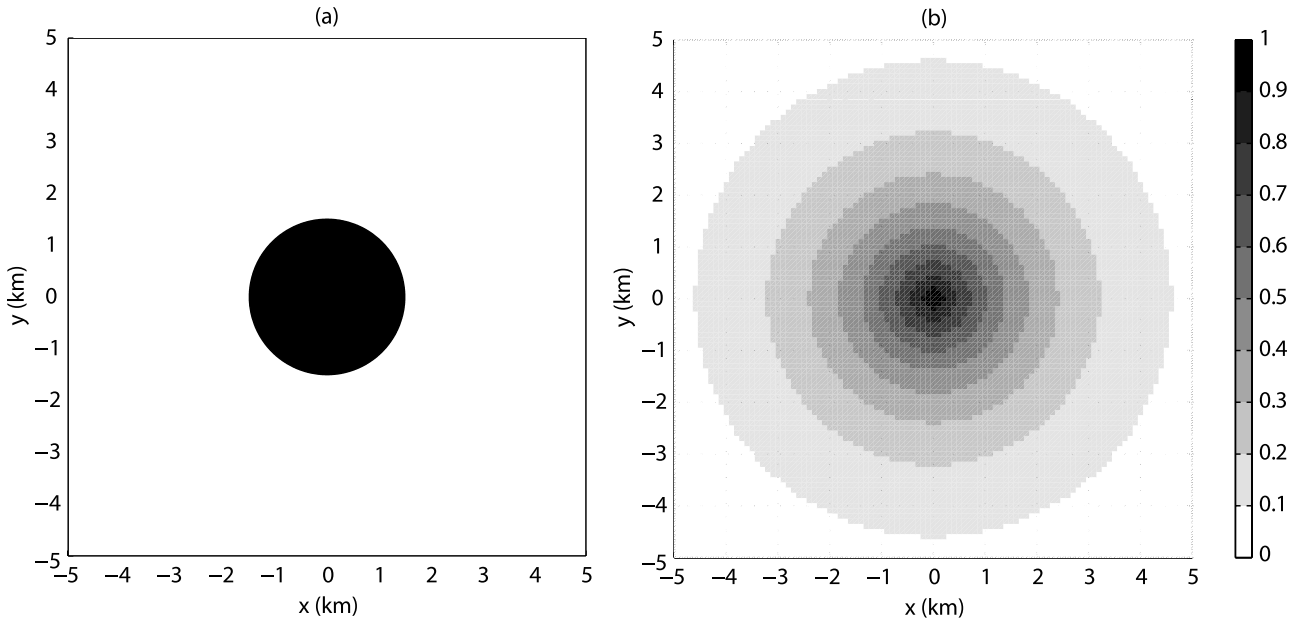


**Figure 7.** Spatial correlation functions in (a) least-squares fitting (UWLS and WLS) ($d_0$ = 1.5 km) and (b) optimal interpolation (OI) ($d_0$ = 5 km and $\lambda_x = \lambda_y$ = 2 km).

grid points is less than 150 m, which is a tenth of the range resolution ($\Delta s$). The correlation coefficients of these pairs with 2 years time span are shown as a function of the difference of bearing angles in Figure 6a. They are distributed somewhat like the cosine function of the difference between bearing angles ($\gamma^2 = 0$), which is the expected value for ideal radial velocity measurements.

[45] In a similar way, the average measurement uncertainty ($\gamma^2$) of the radial velocity can be estimated by assuming that two radial velocities ($r_1$ and $r_2$) are measured by two different radars at the same time for the same current field (equations (44) and (45)):

$$u_1 = u_2 = u \text{ and } v_1 = v_2 = v. \tag{49}$$

[46] The variance of the sum of the two radial velocities is a function of the difference of the bearing angle if $u$ and $v$ are independent:

$$\langle (r_1 + r_2)^2 \rangle = \langle u^2 \rangle (\cos\theta_1 + \cos\theta_2)^2 + \langle v^2 \rangle (\sin\theta_1 + \sin\theta_2)^2 + \langle \epsilon_1^2 \rangle + \langle \epsilon_2^2 \rangle. \tag{50}$$

[47] If the current variance and the error variance in the $x$- and $y$-directions are the same (isotropic current field), respectively:

$$\langle u^2 \rangle = \langle v^2 \rangle = \sigma^2 \text{ and } \langle \epsilon_1^2 \rangle = \langle \epsilon_2^2 \rangle = \gamma^2, \tag{51}$$

the variance of the sum of the radial velocities is

$$\langle (r_1 + r_2)^2 \rangle = 4\,\sigma^2 \cos^2\left(\frac{\theta_1 - \theta_2}{2}\right) + 2\,\gamma^2, \tag{52}$$

where $\sqrt{2}\gamma$ is the RMS error of the sum of oppositely directed radial velocities ($|\theta_1 - \theta_2| = \pi$). From the observations of the nearby radial velocity pairs, the current variance and the error variance are estimated using least-squares fitting, and their square roots are 13.5 and 5.5 cm $s^{-1}$, respectively (Figure 6b). Although this assumes the surface current field has uniform and unpolarized variability, these can be used as the averages for the radial velocity measurements in the study domain. Therefore the average measurement uncertainty ($\gamma^2$) of the radial velocity is assumed to be 30 $cm^2\ s^{-2}$.

## 4. Results

[48] Un-weighted least-squares fitting (UWLS), weighted least-squares fitting (WLS), and optimal interpolation (OI) are applied to the hourly radial velocities over a one month

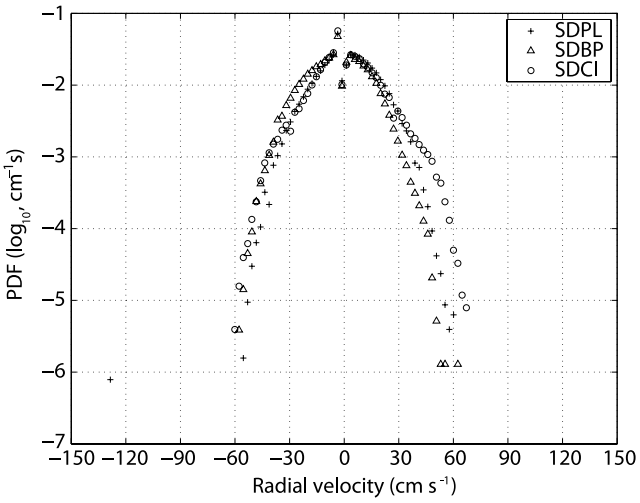


**Figure 8.** PDFs of the radial velocities at each radar site during one month (May 2004).

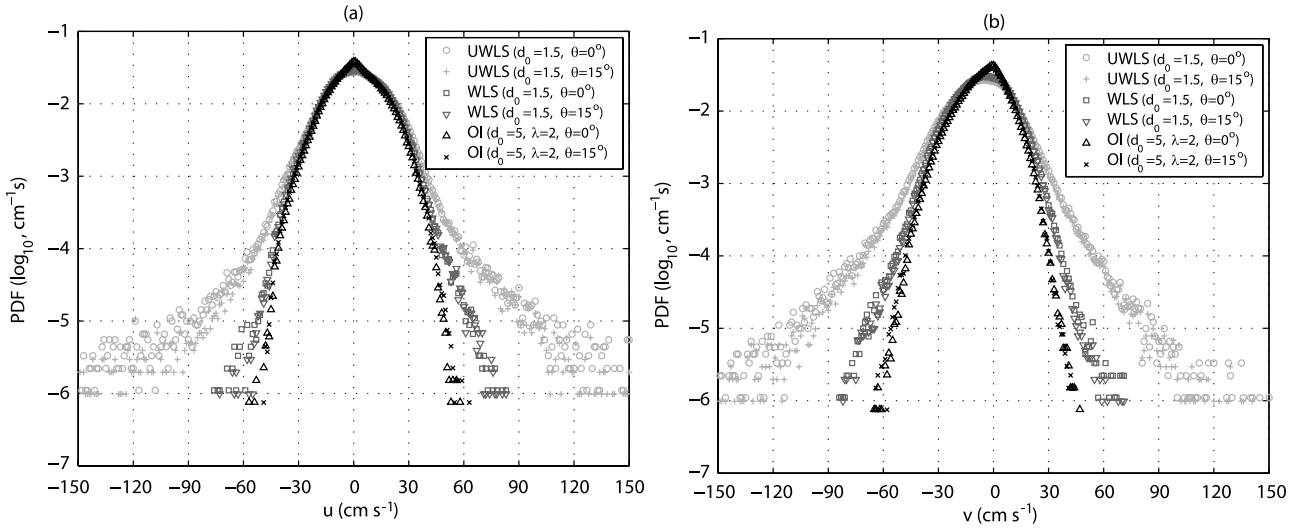


**Figure 9.** PDFs of the vector current components ($u$ and $v$) estimated from the radial velocities during one month (May 2004) using each method (UWLS, WLS, and OI). $d_0$ denotes the search radius and $\theta$ is the swath width for angular interpolation (No angular interpolation is done, if $\theta$ is equal to zero degree). (a) $u$-component. (b) $v$-component.

period (May 2004) in order to examine the estimated vector currents (section 4.3), their uncertainties (section 4.4), the effects of angular interpolation (section 4.5), and the calculation time and noise levels (section 4.6) under the assumed parameters. This one month dataset has fewer missing data than those during other time periods, which allows a better estimate of the vector current and gives an upper bound on calculation time. The three methods are classified by the nature of the singularity in the inversion of the covariance matrix and the structure of the correlation function (Table 1).

### 4.1. Parameter Selection

[49] The search radius ($d_0$) in the UWLS and WLS methods is set to 1.5 km, which is the same as the radar range resolution ($\Delta s$). The segmented correlation function is shown in Figure 7a. The signal variance ($\sigma_s^2$) for the UWLS method is infinite and the error variance ($\sigma_r^2$) is implied as 1 cm$^2$ s$^{-2}$ from $\mathbf{R} = \mathbf{I}$ (equation (5)). In the WLS method, the signal variance and the error variance are assumed the same as the OI method as below.

[50] The correlation function for the OI method is chosen as an exponential function based on the spatially averaged correlation coefficients of surface currents [*Kim et al.*, 2007]. In order to avoid smoothing the estimated current field, the decorrelation length scales of the spatially averaged correlation coefficients are considered to be an upper bound, which are 10–14 km in $u$ and 16–35 km in $v$. The decorrelation length scales ($\lambda_x$ and $\lambda_y$) in the $x$- and $y$-directions of the correlation function in the OI method are chosen to be 2 km, respectively, twice the 1 km vector grid resolution ($\Delta x$ and $\Delta y$). The vector current estimated using the exponential correlation function is less sensitive to the decorrelation length scale than that with Gaussian correlation function, because the exponential correlation falls off more quickly from the center. The exponential correlation function is shown in Figure 7b. For simplicity in the estimate of the surface current field the decorrelation length scales are assumed as a constant in space and all frequency bands. The variation of decorrelation length scales in space and frequency bands can be addressed with the complete data set of estimated vector currents.

[51] The search radius ($d_0$) in the OI method is 5 km, at which range the correlation is 0.08, which can be considered to be a reasonably small spatial weighting. The signal variance ($\sigma_s^2$) and the error variance ($\sigma_r^2$) are assumed to be 400 and 40 cm$^2$ s$^{-2}$, respectively, constant over the observation domain. The error variance ($\sigma_r^2$, equation (13)) is the sum of the average measurement uncertainty ($\gamma^2 \approx 30$ cm$^2$ s$^{-2}$, section 3.3) and the average standard error of the surface currents ($\epsilon^2/N \approx 9$ cm$^2$ s$^{-2}$, section 3.2). This tends to overestimate the error variance because the average standard error contributes to the average measurement uncertainty, but this produces estimates that err on the side of smoothness.

### 4.2. Radial Velocities

[52] The PDFs of the radial velocities measured by each radar site during a one month period (May 2004) are shown in Figure 8. Most radial velocities have magnitudes less than 70 cm s$^{-1}$. One radial velocity with magnitude greater than 90 cm s$^{-1}$ was measured by the SDPL site. The bin size of PDFs is the same as the resolution of radial velocity ($\Delta r$). The PDFs also show consistent discontinuities where the magnitude of radial velocity is less than 2 cm s$^{-1}$ (Figure 4a).

### 4.3. Extracted Vector Currents

[53] The PDFs of the vector current components ($u$ and $v$) estimated using the UWLS, WLS, and OI methods without angular interpolation are compared in Figure 9 (Section 4.5 will explore the effects of angular interpolation of the radial velocity before mapping). The PDFs of the estimated vector components using the OI method are almost the same as the PDFs of radial velocities during the same period (Figure 8). However, the PDFs of the estimated vector components using the least-squares fitting (WLS and UWLS) methods deviate from the PDFs of the OI method at a current

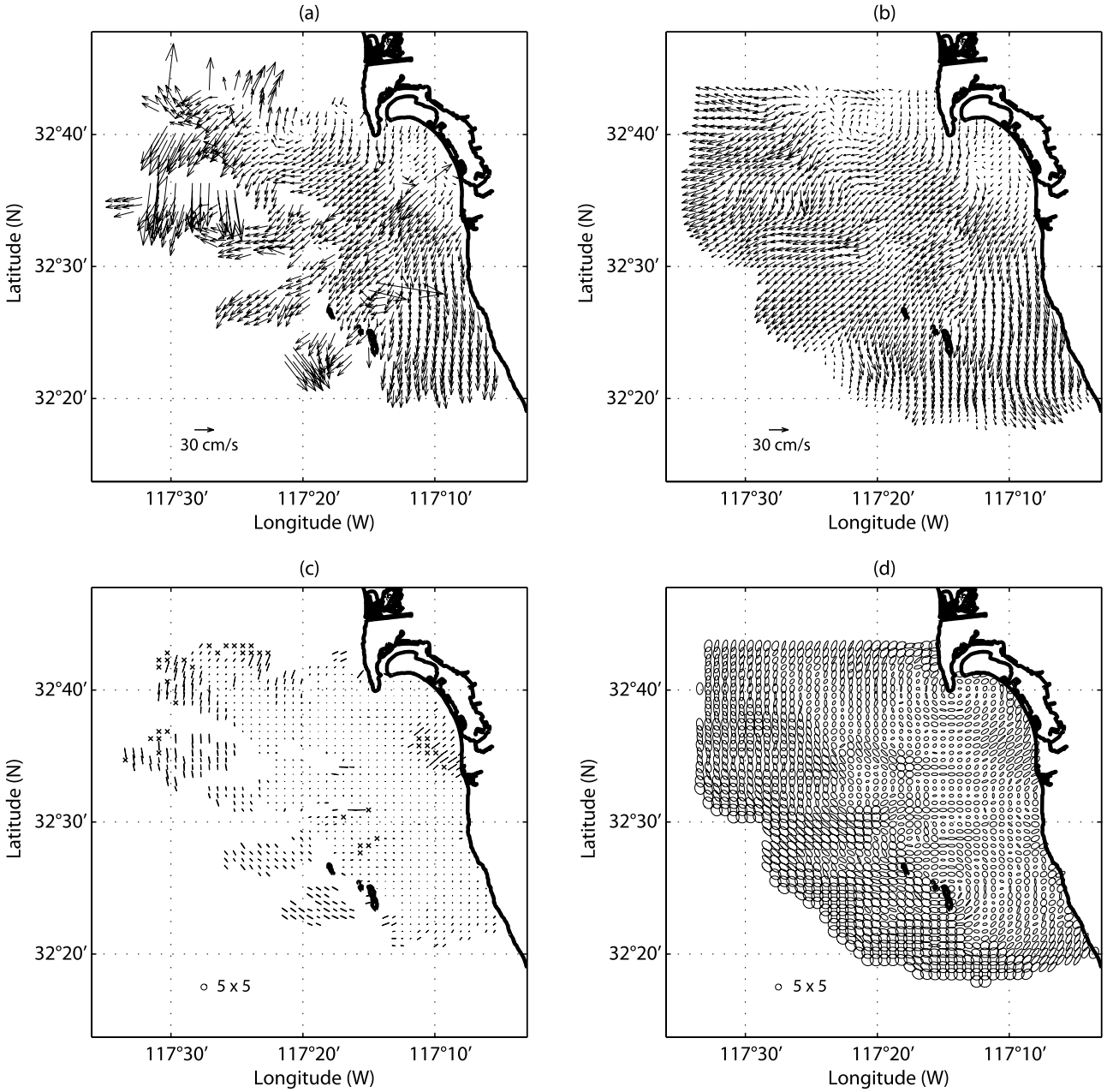


**Figure 10.** An example of the surface vector current field estimated using (a) the UWLS method ($d_0$ = 1.5 km) and (b) the OI method with the assumed error covariance matrix ($d_0$ = 5 km, $\lambda_x = \lambda_y$ = 2 km, $\sigma_s^2$ = 400 cm$^2$ s$^{-2}$, and $\sigma_r^2$ = 40 cm$^2$ s$^{-2}$). (c) and (d) are normalized uncertainty ellipses corresponding to (a) and (b), respectively. The vector grid points having the error level greater than the cut-off error level are indicated with cross marks.

magnitude of about 45 cm s$^{-1}$. These vector components take up about 0.8 and 1.6% (UWLS) and 0.1 and 0.2% (WLS) of the number of total vector components for $u$ and $v$, respectively. They are clustered in the areas having higher GDOP, which are the edges of the coverage of radars and the baselines. The WLS method removes the singularity of the geometric covariance matrix, but is still vulnerable to large errors in the radial velocities. Using a larger search radius in the WLS method reduces them, but generates too smooth a current field. The OI result is less sensitive to the error variance because of the larger averaging region. The OI method yields significantly more zero magnitudes than the UWLS and WLS methods, because the estimator tends to zero where there is insufficient data.

[54] An arbitrarily chosen example of a vector current field estimated from the radial velocities using the UWLS and OI methods is shown in Figures 10a and 10b, respectively. When the number of radial velocities at a given vector grid point is insufficient to extract the vector current (e.g., near baselines and at the edges of the observation domain), the UWLS approach consistently yields inconsistent vectors as shown in Figure 10a, and the OI method tapers the solutions toward zero as shown in Figure 10b. The effective coverage area, defined by the spatial region in

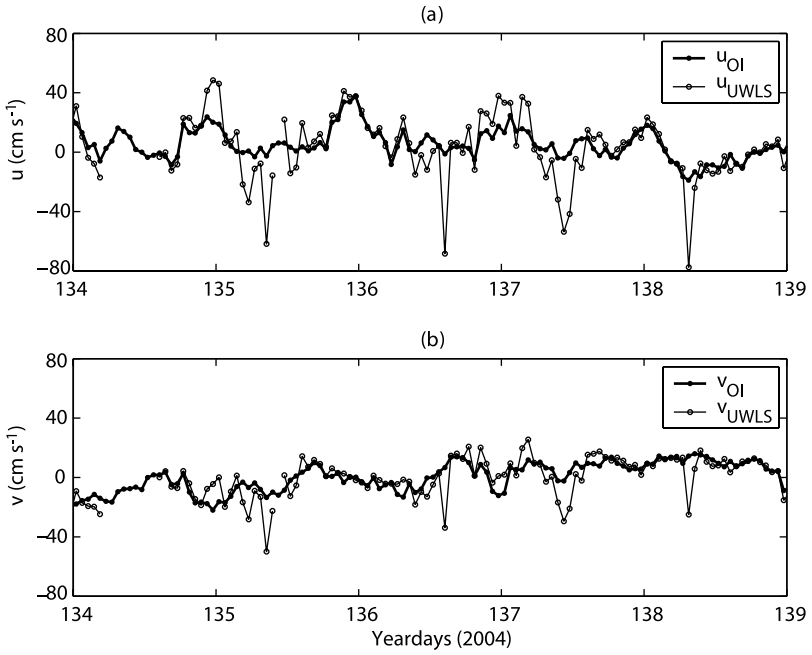


**Figure 11.** An example of the vector current time series estimated using the OI (closed) and UWLS (open) methods. The grid point is located at 32° 35.72′N 117° 10.56′W, which is the one of grid points on the baseline between SDPL and SDBP sites in a nearshore region with about 20 m water depth. (a) *u*-component. (b) *v*-component.

which vector solutions are generated, is found to vary with the mapping method, with the OI method yielding 30–40% more vector current solutions than the UWLS method when using the same input data sets. In addition, the OI method generates smoother current fields than the UWLS method. The number and magnitude of the outliers along the baselines (SDBP and SDPL, SDPL and SDCI) are reduced in the current field estimated by the OI method, because of the nonsingularity in the matrix inversion due to the added error variance and the contribution of the nonparallel radial velocities within the search radius. Although the baseline consistency can be improved in the WLS method, its correlation function is segmented and differs from the observed correlation.

[55] An example of vector current time series estimated using the UWLS and OI methods is shown in Figure 11. The location of the grid point is 32° 35.72′N 117° 10.56′W, which is on the baseline between SDPL and SDBP sites in a nearshore region with about 20 m water depth. The vector components estimated using the UWLS method have both missing and spurious data. On the other hand, the vector components estimated using the OI method show the smoothly-varying current variance and improved consistency on the baseline.

[56] A series of maps estimated using the OI method with the actual HSTD for each radar cell at each time did not seem to differ greatly from the maps estimated with the assumed error variance. However, the OI method using the actual HSTD enables us to make the most use of the available observations.

### 4.4. Uncertainties

[57] The uncertainty in the surface current measurements of the high-frequency radar usually results from the observation errors, the vector current estimation, and the radar system itself such as the misalignment and the poor radar frequency signal-to-noise-ratio [*Graber et al.*, 1997; *Lipa*, 2003]. The uncertainty estimated from the comparison with independent in situ observations is not included in this paper; the discussion focuses on how the uncertainty of the radial velocities is propagated into the uncertainty of the vector currents.

[58] Since the error variances ($\sigma_r^2$) in the UWLS and OI methods are 1 and 40 cm$^2$ s$^{-2}$, respectively, a rescaling of the uncertainty is required to compare the uncertainties ($\varphi$) of the UWLS and OI methods (equations (29) and (28)). Three normalized uncertainty components ($\varphi^{uu}$, $\varphi^{vv}$, and $\varphi^{uv}$) are illustrated with ellipses in Figures 10c and 10d. The cross term ($\varphi^{uv}$) provides the directional uncertainty. The cut-off error level, which is defined by the ratio of the a posteriori uncertainty matrix ($\hat{\mathbf{P}}$) to the expected observational error variance ($\sigma_r^2$), is used as the upper limit of the normalized uncertainty in the UWLS method. The grid points having errors greater than the cut-off error level are indicated by the cross marks in Figure 10c, and are typically near baselines and at the edges of the radar coverage region. The ellipses in Figure 10d are larger than those in Figure 10c, which shows that the OI method has greater uncertainty. However, the uncertainties of the UWLS and OI methods have different statistics (e.g., PDFs as shown in Figure 12) based on different signal and error variance assumptions. In other words, the uncertainty ($\varphi$) normalized by the error variance is only comparable at the lower uncertainty levels, and differs at the higher levels. Because the normalized uncertainty in the UWLS and OI methods varies zero to infinite and zero to the ratio of the signal variance to the error variance, respectively.

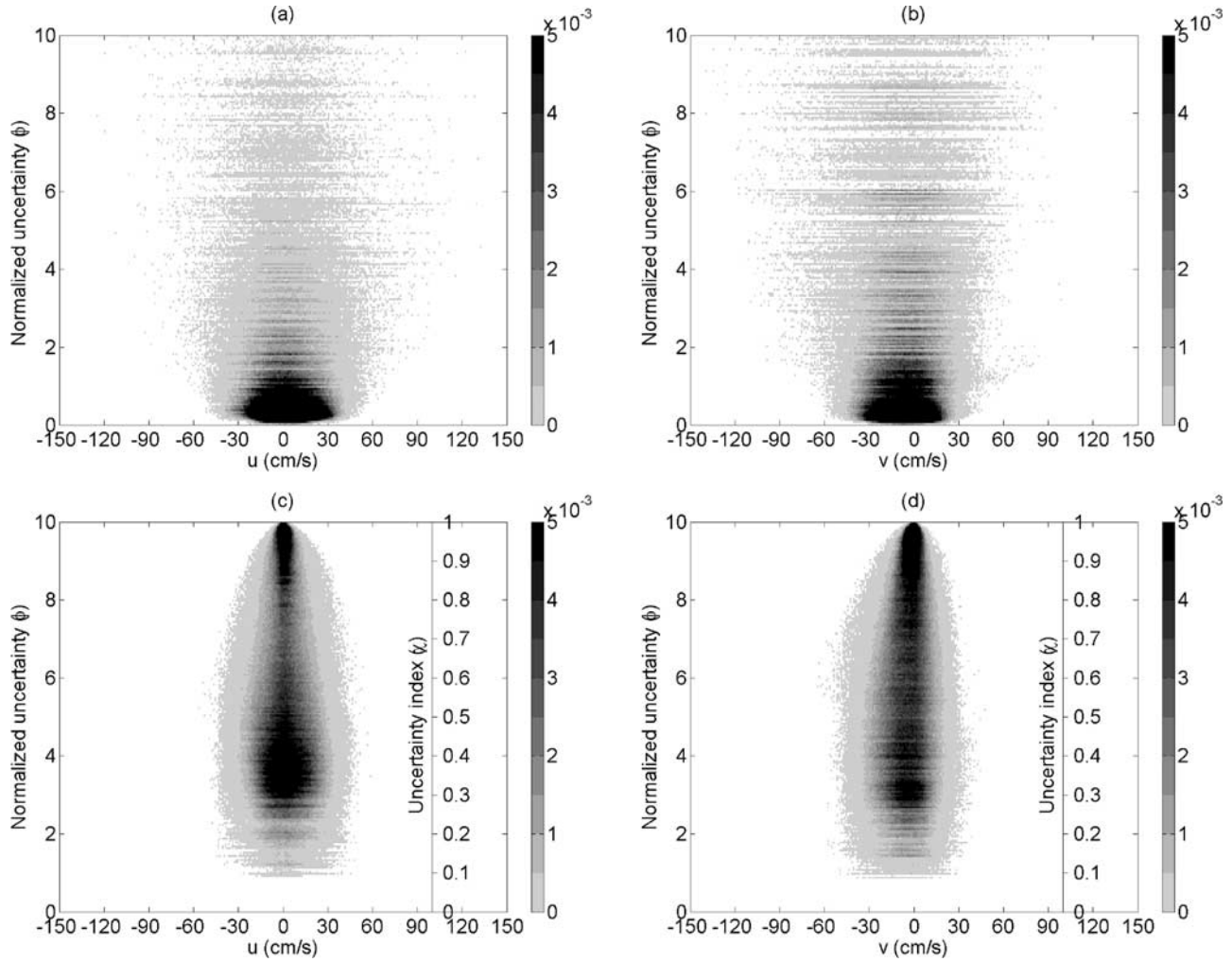


**Figure 12.** Two-dimensional joint PDFs of the vector current components ($u$ and $v$) and their normalized uncertainties ($\varphi^{uu}$ and $\varphi^{vv}$) during one month (May 2004). The assumed axis is for the uncertainty index ($\hat{\chi}$). (a) $\varphi^{uu}$ and $u$ (UWLS). (b) $\varphi^{vv}$ and $v$ (UWLS). (c) $\varphi^{uu}$ and $u$ (OI). (d) $\varphi^{vv}$ and $v$ (OI).

[59] The two-dimensional joint PDFs of the normalized uncertainty and estimated vector current components ($u$ and $v$) for the UWLS and OI methods are shown in Figure 12. The normalized uncertainties greater than the cut-off error level in the UWLS method are not shown in Figures 12a and 12b, and take up about 1.3 and 3.6% of the number of total vector current solutions during a month for $u$ and $v$, respectively. There is no obvious relationship between the normalized uncertainty and the magnitude of the estimated current components. However, the outliers due to singularity of the geometric covariance matrix in the UWLS method have higher normalized uncertainty (Figures 12a and 12b). The current components with higher uncertainty in the OI method are clustered near zero magnitude (Figures 12c and 12d). This is an important positive feature of the OI method.

[60] A new set of uncertainty indices ($\hat{\chi}$), composed of three components ($\hat{\chi}^{uu}$, $\hat{\chi}^{vv}$, and $\hat{\chi}^{uv}$) of the a posteriori uncertainty matrix normalized by the signal variance ($\sigma_s^2$), have values approaching zero for an estimate with zero uncertainty and one for an estimate with no information. The ellipse can be tilted, which represents the directional uncertainty that results from the GDOP at a given vector grid point. The uncertainty indices ($\hat{\chi}^{uu}$ and $\hat{\chi}^{vv}$) in the UWLS method have Rayleigh distributions, which typically represent two orthogonal components with normal and independent distributions. The uncertainty indices ($\hat{\chi}^{uu}$ and $\hat{\chi}^{vv}$) in the OI method have uneven bimodal distributions, which have a higher peak near the center and a lower peak at the end, and the cross-term ($\hat{\chi}^{uv}$) has an exponential distribution. Moreover, the uncertainty indices vary in time except that higher uncertainty indices occur consistently around baselines and at the edges of the domain.

### 4.5. Effects of Angular Interpolation

[61] A commonly used process to fill gaps in MUSIC-derived radial velocity data is to interpolate (or average) across a 15° swath using a boxcar filter. The vector currents estimated from the radial velocities preprocessed with a 15° angular interpolation as well as their uncertainties are considered on the UWLS and OI methods during the analysis period. The angular interpolation increases the spatial extent of the vector currents estimated by the UWLS method. For example, the 15° angular interpolation typically increases the number of good estimates by 10%. However, the angular interpolation is found not to generate any appre-

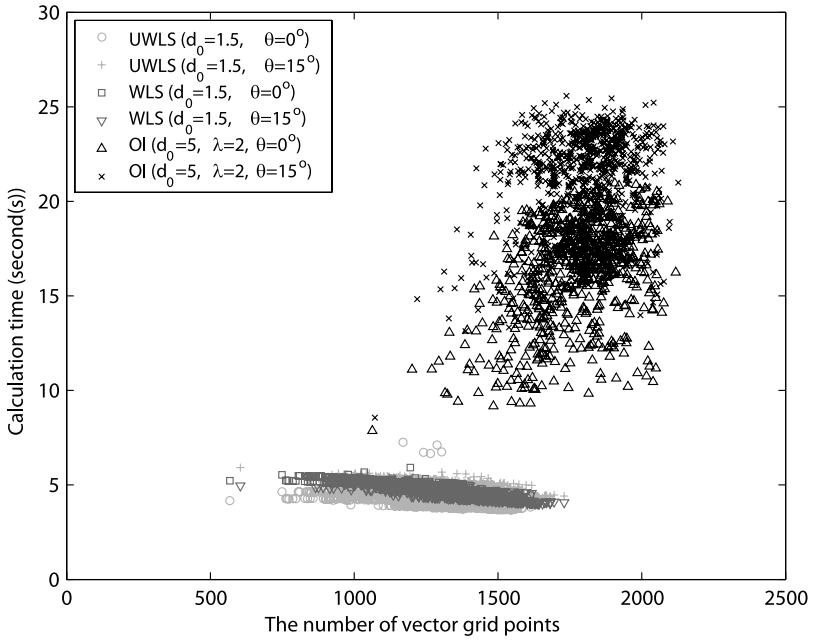


**Figure 13.** Calculation time and the number of vector grid points resolved from the radial velocities during one month (May 2004) using each method (UWLS, WLS, and OI). $d_0$ denotes the search radius and $\theta$ is the swath width of angular interpolation (No angular interpolation is done, if $\theta$ is equal to zero degree).

ciable change in spatial coverage for the OI method. In addition, the angular interpolation is not consistent with the assumptions of the statistics of the field, and does not provide the uncertainty (HSTD).

### 4.6. Calculation Time and Noise Levels

[62] The calculation time for each method (UWLS, WLS, and OI) to estimate the hourly vector current field is shown in Figure 13. On a per-grid point perspective, the calculation time depends on the size of the square matrix to be inverted, which is equal to the number of available radial velocities within the defined search radius in the OI method and two in the least-squares fitting (UWLS and WLS) method (geometric covariance matrix in equation (6)). For a dual Xenon 3.2 GHz processor computer with 2 gigabytes of RAM, the OI method takes about 0.0125 seconds per grid point, which is approximately three times longer than the least-squares fitting method. The calculation time of the OI method is reasonable for modern computers dedicated to real-time monitoring of hourly surface currents.

[63] In order to examine the high frequency noise, the frequency-bin-averaged power spectra of vector current

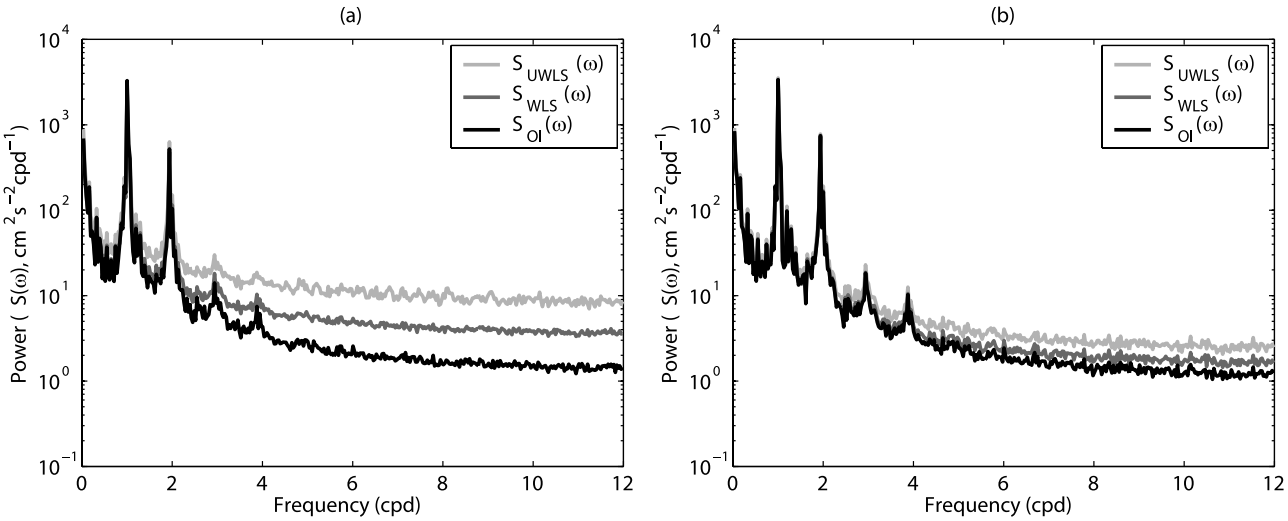


**Figure 14.** Frequency-bin-averaged power spectra of the surface vector current magnitudes estimated using the UWLS, WLS, and OI methods during the 2-year study period over the area with (a) 45% fractional data availability (1337 vector grid points) and (b) 90% fractional data availability (510 vector grid points).

magnitudes estimated using the UWLS, WLS, and OI methods in areas with low and high fractional data availabilities (45 and 90%) over the entire 2-year period are considered, and they are shown in Figures 14a and 14b, respectively. At high frequencies (greater than 8 cycles per day, cpd), the power spectrum of the OI method goes flat at about 10 cpd, while that of the UWLS method is closer to about 8 cpd. However, the amount of variance at frequencies less than 2.5 cpd, which explains most of the variance of the surface currents in the study domain, is almost identical for all three methods.

[64] We assume that the difference between UWLS and WLS is only significant for incompatible or poorly determined points (e.g., the vector currents estimated in the poor GDOP areas), so the difference between these spectra should represent errors. The difference between WLS and OI results from both noise and small scale variance removed by spatial smoothing. We also assume that the variances in the frequency band above about 6 cpd contain only noise. The average noise levels in the area with over 45% coverage are about 8.92, 3.51, and 1.44 $cm^2\ s^{-2}\ cpd^{-1}$ for the UWLS, WLS, and OI methods, respectively, which correspond to 10.34, 6.49, and 4.15 cm $s^{-1}$ standard deviations. The vector current data with 45% coverage have higher errors than the data with 90% coverage, because they have more missing data in areas of marginal coverage and have outliers. In the area of with 45% coverage, the power spectra of the WLS and OI methods differ above about 2 cpd, while in the 90% coverage region, they only differ above about 5 cpd. This suggests that the OI method is not significantly smoothing the current field and is reducing the noise level. The average noise levels in the area with over 90% coverage are 5.62, 4.48, and 3.82 cm $s^{-1}$, respectively. Thus the assumed error variance ($\sim$6.3 cm $s^{-1}$, section 4.1) is acceptable compared to the noise levels of the OI method in both cases (45 and 90% fractional data availabilities).

## 5. Discussions and Conclusions

[65] In the computation of vector currents from radial velocities measured by multiple high-frequency radars, the optimal interpolation (OI) method is suggested as a method to replace the un-weighted least-squares fitting (UWLS) method. The OI method use realistic correlation functions and the HSTD of the radial velocities, resolves the baseline inconsistency, and provides statistically consistent and well-defined uncertainty and increased coverage area. Moreover, the OI method produces currents with a similar PDF to that of the PDF of the radial velocities. The power spectrum of vector currents estimated using the OI method shows a lower level of high-frequency noise than the UWLS method, which is consistent with the assumed error variance.

[66] The OI method can directly calculate the vector currents, the divergence and vorticity of surface currents from the radial velocities, and eliminate the need for multiple mapping steps for the subsequent applications of surface currents. The computational expense of the OI method is reasonable for supporting real-time observation system, even the size of Southern California (about 300 $\times$ 300 $km^2$ region). The continuity equation and boundary conditions can be applied as constraints of the OI method, but this is beyond the scope of this paper.

[67] Although the covariance matrix used for the OI method is often derived from an isotropic spatial correlation function, the observed (possibly smoothed) covariance matrix of the surface currents [*Kim et al.*, 2007] can be used, or a covariance representing a sum of normal modes [*Lipphardt et al.*, 2000; *Kaplan and Lekien*, 2007]. The variability of the estimated vector currents is weakly sensitive to the assumptions of the cut-off error level and the decorrelation length scales of the correlation function. Lower cut-off error level and longer decorrelation length scales generate vector currents with the reduced variability and a spatially smoother field.

## Appendix A: Geometric Dilution of Precision (GDOP)

[68] The geometric dilution of precision (GDOP) is defined as the diagonal components of the inverse of the geometric covariance matrix. The GDOP at a vector grid point generated by the $L$ radial velocities is

$$\left(\mathbf{G}_\mathbf{a}^\mathrm{T}\mathbf{G}_\mathbf{a}\right)^{-1} = \begin{bmatrix} \alpha_{uu} & \alpha_{uv} \\ \alpha_{vu} & \alpha_{vv} \end{bmatrix}, \tag{A1}$$

where $\alpha_{uu}$ and $\alpha_{vv}$ are the GDOP components in the $x$- and $y$- directions ($u$ and $v$), respectively, and $\alpha_r$ is the GDOP of the total current:

$$\alpha_{uu} = \frac{1}{det\left(\mathbf{G}_\mathbf{a}^\mathrm{T}\mathbf{G}_\mathbf{a}\right)} \sum_{l=1}^{L} \sin^2\theta_l \geq \frac{1}{L}, \tag{A2}$$

$$\alpha_{vv} = \frac{1}{det\left(\mathbf{G}_\mathbf{a}^\mathrm{T}\mathbf{G}_\mathbf{a}\right)} \sum_{l=1}^{L} \cos^2\theta_l \geq \frac{1}{L}, \tag{A3}$$

and

$$\alpha_r = \alpha_{uu} + \alpha_{vv} \geq \frac{4}{L} \tag{A4}$$

(*det* denotes the determinant of the matrix). The GDOP depends on the number of available radial velocities within the search radius and their bearing angles. For an appropriate comparison of the GDOP, the GDOP should be normalized with the lowest GDOP in 2-dimensional space [*Levanon*, 2000].

[69] In the case of two radial velocities, the GDOP components are

$$\alpha_{uu} = \frac{\sin^2\theta_1 + \sin^2\theta_2}{\sin^2(\theta_1 - \theta_2)} \geq \frac{1}{2}, \tag{A5}$$

$$\alpha_{vv} = \frac{\cos^2\theta_1 + \cos^2\theta_2}{\sin^2(\theta_1 - \theta_2)} \geq \frac{1}{2}, \tag{A6}$$

and

$$\alpha_r = \frac{2}{\sin^2(\theta_1 - \theta_2)} \geq 2, \tag{A7}$$

respectively.

[70] In the same way, the GDOP components by three radial velocities are

$$\alpha_{uu} = \frac{\sum \sin^2 \theta_l}{det\left(\mathbf{G}_\mathbf{a}^\mathrm{T}\mathbf{G}_\mathbf{a}\right)} \geq \frac{1}{3}, \tag{A8}$$

$$\alpha_{vv} = \frac{\sum \cos^2 \theta_l}{det\left(\mathbf{G}_\mathbf{a}^\mathrm{T}\mathbf{G}_\mathbf{a}\right)} \geq \frac{1}{3} \tag{A9}$$

and

$$\alpha_r = \frac{3}{det\left(\mathbf{G}_\mathbf{a}^\mathrm{T}\mathbf{G}_\mathbf{a}\right)} \geq \frac{4}{3}, \tag{A10}$$

respectively.

[71] The GDOP in high-frequency radar measurements is more localized and time dependent due to the sparse solutions of the MUSIC algorithm compared to the GDOP in satellite remote sensing.

[72] **Acknowledgments.** Sung Yong Kim is supported by the Coastal Ocean Currents Monitoring Program (COCMP). Eric Terrill is supported through funding provided by the Office of Naval Research, NOAA, and the State of California. The observing system infrastructure used in this research was supported by the California Clean Beaches Initiative and its continued operation is provided by both the State of California under COCMP and through NOAA under a grant to develop the Southern California Coastal Ocean Observing System (http://sccoos.ucsd.edu). Bruce Cornuelle is supported by both NOAA (NOAA Award NA17RJ1231) and COCMP. Mark Otero, Lisa Hazard, Paul Reuter, and Tom Cook were responsible for the surface current data acquisition, and Daniel Birch gave insightful comments on the draft.

## References

Barrick, D. E., and B. J. Lipa (1996), Phase 1 SBIR Final Report: Comparison of direction-finding and beam-forming in HF radar ocean surface current mapping, *Tech. Rep.*, Nat'l. Ocean. and Atmos. Admin., Rockville, MD.

Barrick, D. E., and B. J. Lipa (1997), Evolution of bearing determination in HF current mapping radars, *Oceanography*, *10*(2), 72–75.

Bretherton, F. P., R. E. Davis, and C. B. Fandry (1976), A technique for objective analysis and design of oceanographic experiment applied to MODE-73, *Deep Sea Res.*, *23*, 559–582.

Chapman, R. D., L. K. Shay, H. Graber, J. B. Edson, A. Karachintsev, C. L. Trump, and D. B. Ross (1997), On the accuracy of HF radar surface current measurements: Intercomparisons with ship-based sensors, *J. Geophys. Res.*, *102*(C8), 18,737–18,748.

Daley, R. (1993), Estimating observation error statistics for atmospheric data assimilation, *Ann. Geophys.*, *11*, 634–647.

Davis, R. E. (1985), Objective mapping by least squares fitting, *J. Geophys. Res.*, *90*(C7), 4773–4778.

de Paolo, T., and E. Terrill (2007), Skill assessment of resolving ocean surface current structure using compact-array-style HF radar and the MUSIC direction-finding algorithm, *J. Atmos. Ocean. Technol.*, *24*, 1277–1300, doi:10.1175/JTECH2040.1.

Golub, G. H., and Van C. Loan (1996), *Matrix Computations*, 3rd ed., The Johns Hopkins Univ. Press, Baltimore, MD.

Graber, H. C., B. K. Haus, R. D. Chapman, and L. K. Shay (1997), HF radar comparisons with moored estimates of current speed and direction: Expected differences and implications, *J. Geophys. Res.*, *102*(C8), 18,749–18,766.

Gurgel, K.-W. (1994), Shipborne measurements of surface current fields by HF radar, *L'Onde Electr.*, *74*(5), 54–59.

Kaplan, D. M., and F. Lekien (2007), Spatial interpolation and filtering of surface current data based on open-boundary modal analysis, *J. Geophys. Res.*, *112*, C12007, doi:10.1029/2006JC003984.

Kim, S. Y., E. J. Terrill, and B. D. Cornuelle (2007), Objectively mapping HF radar-derived surface current data using measured and idealized data covariance matrices, *J. Geophys. Res.*, *112*, C06021, doi:10.1029/2006JC003756.

Levanon, N. (2000), Lowest GDOP in 2-D scenarios, *IEE Proc., Radar, Sonar Navig.*, *147*, 149–155.

Lipa, B. J. (2003), Uncertainties in SeaSonde current velocities, paper presented at IEE/OES Seventh Working Conference on Current Measurement Technology, Inst. of Elctr. and Electron. Eng., San Diego, Calif.

Lipa, B. J., and D. E. Barrick (1983), Least-squares methods for the extraction of surface currents from CODAR crossed-loop data: Application at ARSLOE, *IEEE J. Ocean. Eng.*, *8*(4), 226–253.

Lipphardt, B. L., Jr., A. D. Kirwan Jr., C. E. Grosch, J. K. Lewis, and J. D. Paduan (2000), Blending HF radar and model velocities in Monterey Bay through normal mode analysis, *J. Geophys. Res.*, *105*(C2), 3425–3450.

Lorenc, A. (1986), Analysis methods for numerical weather prediction, *Q. J. R. Meteorol. Soc.*, *112*, 1117–1194.

Schmidt, Roy O. (1986), Multiple emitter location and signal parameter estimation, *IEEE Trans. Antennas Propag.*, *AP-34*(3), 276–280.

Scott, D. (1979), On optimal and data-based histograms, *Biometrika*, *3*(66), 605–610.

Wunsch, C. (1996), *The Ocean Circulation Inverse Problem*, Cambridge Univ. Press, New York.

B. D. Cornuelle, Physical Oceanography Research Division, Scripps Institution of Oceanography, 9500 Gilman Drive, La Jolla, CA 92093, USA. (bdc@ucsd.edu)

S. Y. Kim and E. J. Terrill, Marine Physical Laboratory, Scripps Institution of Oceanography, 9500 Gilman Drive, La Jolla, CA 92093, USA. (syongkim@mpl.ucsd.edu; eterrill@ucsd.edu)